Interfacial destabilization and atomization driven by surface acoustic waves

Aisha Qi, Leslie Y. Yeo,[a] and James R. Friend
Micro/Nanophysics Research Laboratory, Monash University, Clayton, Victoria 3800, Australia

Surface acoustic wave atomization is a rapid means for generating micron and submicron aerosol droplets. Little, however, is understood about the mechanisms by which these droplets form due to the complex hydrodynamic processes that occur across widely varying length and time scales. Through experiments, scaling theory, and simple numerical modeling, we elucidate the interfacial destabilization mechanisms that lead to droplet formation. Using a millimeter-order fluid drop exposed to surface acoustic waves as it sits atop a single-crystal lithium niobate piezoelectric substrate, large aerosol droplets on the length scale of the parent drop dimension are ejected through a whipping and pinch-off phenomenon, which occurs at the asymmetrically formed crest of the drop due to leakage of acoustic radiation at the Rayleigh angle. Smaller micron order droplets, on the other hand, are formed due to the axisymmetric breakup of cylindrical liquid jets that are ejected as a consequence of interfacial destabilization. The 10 μm droplet dimension correlates with the jet radius and the instability wavelength, both determined from a simple scaling argument involving a viscous-capillary dominant force balance. The results are further supported by numerical solution of the evolution equation governing the interfacial profile of a sessile drop along which an acoustic pressure wave is imposed. Viscous and capillary forces dominate in the bulk of the parent drop, but inertia is dominant in the ejected jets and within a thin boundary layer adjacent to the substrate where surface and interfacial accelerations are large. With the specific exception of parent drops that spread into thin films with thicknesses on the order of the boundary layer dimension prior to atomization, the free surface of the drop is always observed to vibrate at the capillary-viscous resonance frequency—even if the exciting frequency of the surface acoustic wave is several orders of magnitude larger—contrary to common assumptions used in deriving subharmonic models resulting in a Mathieu equation for the capillary wave motion, which has commonly led to erroneous predictions of the droplet size. © *2008 American Institute of Physics*. [DOI: 10.1063/1.2953537]

I. INTRODUCTION

The generation of micron and submicron aerosol droplets is important to a wide range of industrial processes. Fuel injection in internal combustion engines, ink-jet printing, agricultural sprays, mass spectrometry, pulmonary drug delivery, and DNA microarray printing[1] all rely on dense, monodisperse, and specifically sized aerosols. With subsequent evaporation, biodegradable polymeric micro- and nanoparticles for targeted and controlled release drug delivery represent one of the many ways in which such aerosols may be used to form novel products.[2] Further, immunodiagnostics and amplification of DNA hybridization biosensors—with the recent emergence of novel ways to functionalize the surfaces of such particles—are two vital areas being explored by many researchers. The atomization and subsequent in-flight evaporation of solvent droplets in which polymeric excipients are dissolved is an attractive alternative to the slow and cumbersome multistep conventional methods (e.g., spray drying, nanoprecipitation, emulsion photocross-linking, etc.) for synthesizing these micro- and nanoparticles.[2,3]

Current atomization methods include hydrodynamic flow focusing,[4] electrospraying,[5,6] ultrasonic atomization,[7–9] and vibration-induced atomization,[10,11] among others. Regardless of the method utilized, however, the principal challenge is to develop a technology that is rapid, precise, reliable, reproducible, robust, and controllable for generating monodispersed distributions of liquid aerosol droplets and particles at the micron and nanometer scales. The capillary stress, which scales as γ/R, where γ is the liquid surface tension and R is the characteristic drop dimension, becomes large when R is at micron or submicron length scales; each atomization method above therefore employs one form of external forcing or another—viscous shear, electric field, acoustic field, or inertial vibration in the above examples—to overcome the capillary stabilization mechanism that resists sufficient deformation of the liquid surface and subsequent pinch-off of the liquid thread to permit the formation of an aerosol droplet.

One subset of ultrasonic atomization techniques that is relatively unknown is surface acoustic wave (SAW) atomization.[2,12] SAW atomization is fundamentally different to high-power ultrasonic atomization techniques that use Langevin transducers and single lead zirconium titanate element thickness-mode piston atomizers.[9] First, the frequency of operation of ultrasonic atomizers (20 kHz to 3 MHz) is

---
a)Author to whom correspondence should be addressed. Electronic mail: leslie.yeo@eng.monash.edu.au. Fax: +61 3 9905 4943.

20, 074103-1

one to two orders of magnitude lower than that of SAW atomizers (10–500 MHz). Furthermore, the *applied* power in SAW atomization is at least an order of magnitude smaller, only in part due to the smaller working volume of the atomizing fluid. Finally, the undulating motion of the substrate in SAW atomization is more complex than the simple reciprocating piston motion[9] in ultrasonic atomization techniques. SAW devices are fabricated with integrated circuit photolithographic methods and are, therefore, easily miniaturized,[13] enabling inexpensive mass production of portable drug delivery and point-of-care diagnostics as part of a complete lab-on-a-chip system.

While SAWs have been used for over four decades in the telecommunications industry for rf signal processing and filtering,[14] only recently have they been considered for drop translation,[15] microchannel pumping,[16] drop manipulation,[17] micromixing,[18,19] and microparticle collection[15,20] and concentration,[21] forming specific examples of the potential of this technology, as do lab-on-a-chip devices for microarray technology[22] and rapid bioscaffold cell seeding.[23]

A SAW is a nanometer-order amplitude acoustic wave that propagates along and near the surface of a single-crystal piezoelectric substrate. The wave motion is rapidly attenuated with increasing depth into the substrate and is entirely absent four to five wavelengths into the substrate from the propagation surface. In contrast, a SAW will propagate over thousands of wavelengths of distance—several centimeters—along the surface in a low loss piezoelectric material such as lithium niobate ($LiNbO_3$ or LN). Until White and Voltmer[13] developed patterned metal *interdigital transducer* (IDT) electrodes deposited directly onto the piezoelectric substrate as depicted in Fig. 1(a), generating such waves was problematic. There are many kinds of SAWs, though by far the most commonly used for actuation is the *Rayleigh* wave,[24] a transverse-axial elliptical electroacoustic wave as shown in Fig. 1(a). The x-propagating Rayleigh wave speed on the unloaded 127.68° y-x cut LN substrate c_s is 3965 m/s. At high powers, the displacement velocity of the surface as the SAW passes is on the order of 1 m/s regardless of the excitation frequency, i.e., the SAW frequency. Thus, at excitation frequencies on the order of 10 MHz, we expect the displacement of the surface and the amplitude of the acoustic wave to be only around 10 nm. However, the acceleration of the surface is incredibly high, at around 10^7 m/s². Such huge surface accelerations are transmitted into a liquid drop placed upon it, inducing strong acoustic waves within the drop and capillary waves on the drop free surface that are destabilized with sufficient acoustic excitation. In this way a convenient and useful forcing mechanism for rapid and high throughput atomization is formed.

The diffraction of the SAW into the drop is defined by the difference in wave propagation speeds in the two media; compressional waves in water propagate at $c_w = 1485$ m/s, much less than the SAW propagation speed c_s. This difference causes the SAW to diffract into the water drop at the *Rayleigh angle*[17] $\theta_R = \sin^{-1}(c_w/c_s) \sim 22°$. The acoustic radiation *leaked* into the fluid drop gives rise to a longitudinal pressure wave that, in turn, induces bulk recirculation in the
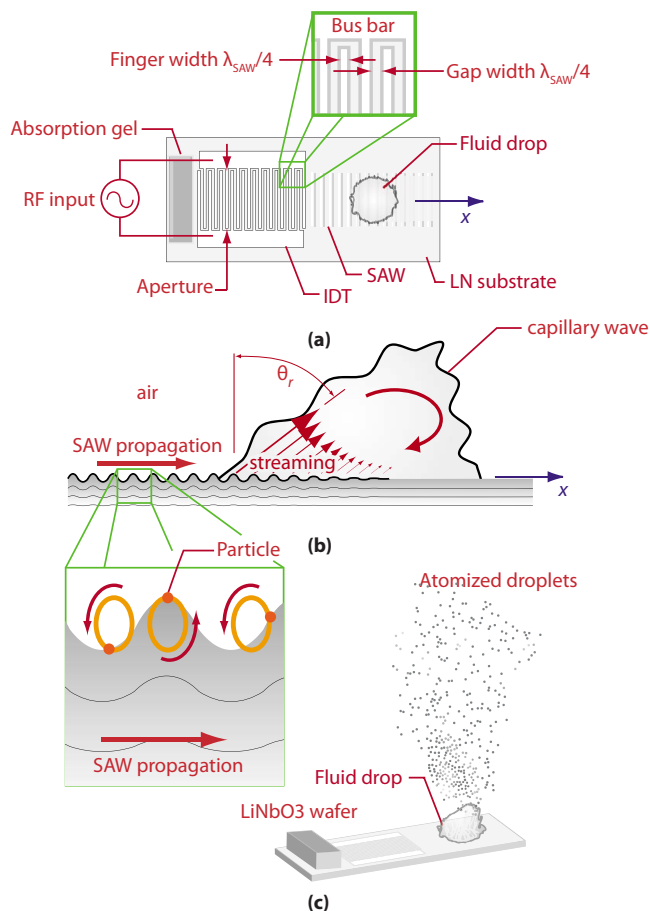

FIG. 1. (Color online) SAW propagation along a piezoelectric substrate. (a) Configuration of the SAW device and the IDT electrode deposited on the piezoelectric substrate to generate the SAW. (b) Interaction of the SAW with a fluid drop causes the drop to deform into an asymmetric conical shape leaning roughly at an angle corresponding to the Rayleigh angle θ_R; the free surface of the drop undulates with a wideband frequency response roughly indicated here with a single wavelength capillary wave. The SAW itself is a retrograde traveling wave: a point on the surface travels in an ellipse in a counterclockwise fashion if the wave moves from left to right. The SAW is largest in amplitude on the surface, decaying exponentially to almost negligible levels within four to five wavelengths below the surface. The acoustic irradiation causes drop deformation through first-order effects on the time scale of the acoustic wave and bulk fluid recirculation on a hydrodynamic time scale, known as *acoustic streaming*, through second-order time-averaged effects. The SAW amplitude is reduced by the interaction with the drop due to the effects of viscous dissipation. (c) Schematic representation of the elliptical trajectory of the particle elements on the surface as the SAW Rayleigh wave traverses the surface. Atomization occurs from the free surface of the irradiated drop.

drop, known as *acoustic streaming* [Fig. 1(b)]. It is this fluid-structural coupling that allows the exploitation of the SAW for the variety of microfluidic manipulations described above.

Our motivation in this paper is the ability to harness this fluid-structural coupling for rapid liquid atomization. While SAW atomization has been demonstrated as a tool for generating micron and submicron aerosol droplets, little is known about the mechanism responsible for droplet generation. Though free surface breakup mechanisms for low-frequency (1 kHz order) vibration-induced atomization based on the parametric excitation of Faraday waves are present in the literature,[11,25] there is no particular reason to

believe that these mechanisms apply to the 10 MHz order SAW atomization process described here. The few SAW and high-frequency (>1 MHz) bulk ultrasonic atomization studies available simply employ a modification of Kelvin's equation for the wavelength λ of the capillary waves induced by periodic vertical forcing,

$$\lambda \sim \left(\frac{2\pi\gamma}{\rho f_c^2}\right)^{1/3}, \tag{1}$$

in which γ and ρ are the interfacial tension and density of the fluid, respectively, and f_c is the frequency of the free surface capillary waves.[26] The frequency of the capillary wave, f_c, is not easy to determine experimentally and the typical approach has been to determine how the capillary wave frequency is related to the external excitation frequency, f.

Traditionally the excitation has been pistonlike, in phase across the width of the fluid and perpendicular to the free surface in a manner identical to that used to study Rayleigh–Taylor surface instabilities.[27] Using this arrangement, many researchers over the years have studied the formation of waves that dominate the surface motion at a subharmonic frequency that is half the excitation frequency, f, and an elegant theory has been constructed around these *Faraday waves*[28] with Mathieu's equation used to describe the selection phenomena[29] and the Hopf bifurcations that appear upon sufficient excitation; Miles and Henderson provided a thorough examination of this area.[30] Based on the ample evidence from experiments using frequencies far below that used in our study and the closely correlated theories associated with them, many researchers have presumed $f_c \approx f/2$ in determining the capillary wavelength:[7,9,31–33]

$$\lambda = \kappa\left(\frac{8\pi\gamma}{\rho f^2}\right)^{1/3}. \tag{2}$$

The only difference between Eqs. (1) and (2) is this implicit assumption that the frequency of the capillary waves on the free surface of the liquid drop is one-half the excitation frequency, i.e., $f_c = f/2$. The coefficient κ has been set to a variety of values in the literature as discussed a bit later but for an order-of-magnitude analysis may be treated as $\kappa \approx 1$.

Curiously, there is a large volume of literature that adheres to this equation while a thoughtful consideration of forces on the capillary waves suggests either

$$f_c \sim \frac{\gamma}{\mu R} \tag{3}$$

as the capillary resonance frequency due to internal viscous damping of the drop[6] or

$$f_c \sim \left(\frac{\gamma}{\rho R^3}\right)^{1/2} \tag{4}$$

as the capillary resonance frequency due to inertial forcing of the drop.[6,34] For a water droplet with viscosity $\mu \sim 10^{-3}$ kg/m s and surface tension $\gamma \sim 10^{-2}$ N/m having a characteristic length scale $R \sim 10^{-2}$–10^{-3} m, the *viscous-capillary resonant frequency* from Eq. (3) is $f_c \sim 1$–10 kHz. With a density of $\rho \sim 10^3$ kg/m^3, the *capillary-inertia resonant frequency* from Eq. (4) is $f_c \sim 10^{-2}$–10^{-1} kHz. Both of

these frequencies are based on the physical behavior of the free surface of the drop, yet neither corresponds to the subharmonic relation $f_c = f/2$. At lower frequencies of excitation, from 20 kHz to 1 MHz, the discrepancy is modest. However, at the frequencies used in SAW atomization, the assumption $f_c = f/2$ (Ref. 31) gives capillary wave frequencies two orders of magnitude higher than what is physically possible. Later, we provide clear experimental evidence demonstrating that there are capillary waves at the frequencies given by Eqs. (3) and (4) but *no* capillary wave at the subharmonic frequency $f_c = f/2$. It would be remarkable indeed if, regardless of the choice of fluid, the subharmonic relationship remained valid given the dispersive nature of the capillary wave and the wide variety of viscosities, densities, and surface tensions exhibited by fluids.

The origin of the half-frequency subharmonic assumption appears to be the work of Faraday,[28] in which he observed this relation in mercury and other fluids and argued the behavior was much like the oscillation of a pendulum. The equations of motion for both physical phenomena can be described as a Mathieu equation,[35] where the phenomena are driven *parametrically* in response to the excitation. Moreover, selection of the lowest-order resonance frequency $f_c = f/2$ from the many available resonances $f/2, 3f/2, 5f/2, \dots$ has been shown to be a consequence of the weak nonlinearity present in low-amplitude capillary waves where analytical techniques can be used to provide useful information.[29,30] From the ingenuity of researchers in these interceding years, the theory describing the weakly nonlinear capillary wave behavior has been thoroughly explained.[30,31,36,37] Unfortunately, Faraday's original assumption appears to have survived despite physical evidence to the contrary. A likely reason is the difficulty in observing the actual motion of the fluid surface, especially at high frequencies where the discrepancy would be obvious.

Here, we return to the original Kelvin equation in Eq. (1) and suggest that its modification in Eq. (2), by replacing the capillary frequency f_c with the excitation frequency f, is unfounded. In fact, we suggest that the proper frequency to use is exactly that in the original Kelvin equation in Eq. (1), i.e., the capillary wave frequency f_c. We show that the use of Eq. (3) or (4) for f_c leads to a good prediction of the instability wavelength and, hence, the approximate size of the atomized droplets. While previous studies[7,9,32,33] have found reasonable correlation between the modified Kelvin equation in Eq. (2) and the resulting atomized droplet diameter, their correlations are often aided by an empirically determined fitting coefficient that varies from study to study—from between 1 and 3.8 by Kurosawa,[32] 0.34 by Lang,[7] and $1/\pi$ by Barreras *et al.*,[33] for example.

The rest of this paper is organized as follows. Scanning laser Doppler vibrometry and high-speed flow visualization were used to directly measure the capillary wave frequency and capture the interfacial destabilization process leading to drop atomization as described in Sec. II. Using simple physical scaling arguments and the results of the experimental work, we postulate the different mechanisms that may be responsible for the atomization. In particular, our emphasis will be based on a discussion of length and time scales in

which we assert that a proper appreciation for the separation of the various length and time scales associated with the problem and the selection of the relevant scale is essential to yield an understanding of the proper physical mechanisms underlying the process. We then proceed in Sec. III to construct a simple thin film lubrication model that enables a transient nonlinear growth analysis of the film height under the influence of a harmonic pressure perturbation at the interface. Unlike previous analyses,[31] we allow for a traveling wave along the fluid drop–solid interface consistent with the form of fluid excitation via SAW that we are making use of in this study. The fourth-order nonlinear film evolution equation arising from the analysis is then solved numerically to show the destabilization of the interface at a critical acoustic capillary number. We conclude by showing that good agreement is obtained between the numerical analysis and the experimental results in both the predicted critical acoustic capillary number at the onset of atomization and the wave number of the dominant instability giving rise to atomized droplets via SAW.

II. EXPERIMENTS

A. Experimental setup and initial observations

SAWs may be generated upon the surface of many materials, though they are conveniently generated on single-crystal piezoelectric materials using IDT electrodes, named after the comblike pattern formed in a thin film of metal atop the piezoelectric substrate [Fig. 1(a)]. An IDT of 25 straight electrode pairs was used in this study; a set of 25 fingers shared a common electrical connection—the *bus bar*—with each 10 mm long finger placed between a similarly shaped set of fingers connected at the opposite end in another bus bar. The IDT was fabricated using standard UV photolithography in a basic full-width interleave configuration constructed from 250 nm thick aluminum atop a 4 nm titanium layer both sputter deposited onto a 127.68° *y-x* cut, *x*-propagating lithium niobate (LN) (Roditi Ltd., London, UK) single-crystal piezoelectric substrate, as schematically described in Fig. 1. When a sinusoidal electrical signal is transmitted across the IDT, a SAW is generated perpendicular to the fingers' long axis and along the *x* axis of the substrate from both apertures (sides) of the IDT. A 1 mm gap between the ends of the fingers and the 3 mm wide bus bar connecting the opposing set of IDT fingers was chosen, giving rise to a SAW 8 mm wide propagating from the apertures. The wavelength of the SAW is defined by the width of the IDT fingers and the gaps' absent metal between these fingers. In the standard straight configuration used here, the gap and finger width were the same at 50 μm and equivalent to one-quarter wavelength of the generated SAW in the LN substrate; the SAW, traveling at a wave speed of 3585 m/s, has a wavelength λ_{SAW} and resonant frequency of 200 μm and 20 MHz, respectively. To maximize the piezoelectric coupling, the input sinusoidal signal was delivered at this same frequency.

By placing a 2 μl water drop directly onto the substrate and completely within the 8 mm wide SAW irradiation region, the application of the input signal into the IDT caused

oscillation of the drop surface. The resulting capillary waves on the free surface of the drop were visualized at high speed using a high-speed video camera (iSpeed, Olympus, Tokyo, Japan) with a frame rate capability of up to 33 000 frames/s connected to a stereomicroscope (BXFM, Olympus, Tokyo, Japan) with 5× and 10× magnifications. Additional illumination to the backlighting provided by the microscope is necessary to visualize the magnified capillary wave at these speeds, and here a fiber optic lamp (Fiber-Lite PL800, Dolan–Jenner, Boxborough, MA) was used for this purpose. A scanning laser Doppler vibrometer (MSA-400, Polytec PI, Waldbrunn, Germany) with fast Fourier transform (FFT) of the measurement signal was used to determine the frequency spectrum of the SAW excitation being provided via the substrate and the capillary wave upon the free surface of the drop. The MSA-400 offers measurements of vibration perpendicular to the substrate surface at up to 40 MHz, ±75 μm, and ±10 m/s in frequency, displacement, and vibration velocity, respectively, and displacement and vibration velocity resolutions of less than 0.1 pm and 1 μm/s, serving as an effective measurement tool for this study. Since the measurement provided by the system is an integrated result of the Doppler shift imposed on the laser radiation while it propagates from the laser head, to the target, and along its return (altogether the measurement leg of the modified Michelson interferometer underpinning the MSA-400), care must be taken to ensure that the frequency spectrum of the capillary waves is obtained independently of the frequency spectrum of the substrate. Fortunately, the MSA-400 uses a finite length He–Ne laser source and so there is a specific coherent length and defined focal plane that may be placed at will along the laser path via a focusing mechanism provided in the laser head, allowing one to choose the actual measurement location at either the substrate or the free surface of the drop. Above a critical value of the input power into the IDT, the drop will atomize, producing micron to submicron aerosol droplets. We measured the droplet size distribution using an aerodynamic particle spectrometer (model 3321, TSI Inc., Shoreview, MN), capable of measuring aerosol droplet sizes between 0.5 and 20 μm using time-of-flight measurements.

Two different forms of atomization are possible depending on the interaction between the drop and substrate. Figure 2 shows the typically dramatic interfacial deformation that occurs as SAW radiation propagates in the LN substrate beneath the drop and a spin-coated 500 nm thick Teflon-AF layer (DuPont Corporation, Wilmington, DE). The hydrophobicity of the Teflon layer on the substrate beneath the drop prevents the drop from spreading. Leakage of SAW radiation from the substrate into the drop at the Rayleigh angle causes the drop to deform into an asymmetric conical shape tilted toward the direction of SAW propagation in the substrate (i.e., along the *x* axis). The long side of the conical shape is at the Rayleigh angle, while capillary waves form on the free surface of the drop. The capillary waves quickly destabilize and elongate to form individual jets, each of which eventually breaks up to form one or more droplets. There is also a "mist" of droplets in the background above the free surface of the parent drop, akin to that seen by Barreras *et al.*[33] We speculate that these mists originate from
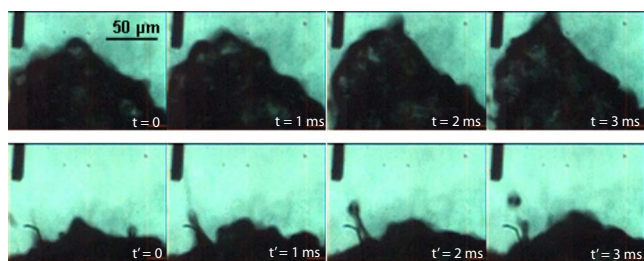
FIG. 2. (Color online) Two sets of image sequences showing drop deformation into an asymmetric conical shape and the rapid destabilization of its free surface leading to atomization of small droplets from the parent drop due to SAW irradiation, acquired at 1000 frames/s and 5× magnification. Both occur above a hydrophobic Teflon coated surface, spin coated above the lithium niobate substrate. In the second case, note the formation of an elongated axisymmetric cylindrical jet at $t'=0$ ms and $t'=1$ ms, which eventually pinches off to form a droplet at $t'=2$ ms and $t'=3$ ms. In both cases, the SAW propagation direction is from the right to the left of the image.

FIG. 4. (Color online) Results from the FFT frequency sweep using the scanning laser Doppler vibrometer showing the frequency at which the capillary wave on the free surface of the drop is excited. (a) Drop with finite thickness of approximately 10^{-4} m: the resonant frequency of the capillary wave is approximately 10 kHz. (b) Thin film of thickness 10^{-6} m: the resonant frequency of the capillary wave is approximately 20 MHz, the exciting frequency.

jets emanating from the drop free surface at many different locations. These jets break up to produce small ejected droplets; since these events occur rapidly across the fluid surface, the multitude of these tiny ejected droplets appear as a mist above the parent drop. Another possibility for the origin of the mist is the secondary breakup of the ejected droplets due to their high inertial energies to form multiple droplets.

In contrast, if the drop were to be placed atop the bare, hydrophilic LN surface, the drop forms a thin film that extends along the propagation direction of the SAW—instead of a tilted conical shape—as observed in Fig. 3. Nevertheless, the capillary waves which destabilize to produce jetting or pinch-off and misting still appear much the same as with the hydrophobic case.

B. Relevant length and time scales

The likely reason for much of the confusion surrounding fluid atomization using acoustic irradiation is the difficulty in observing such phenomena. Even for ultrasonic atomization at modest frequencies (20–40 kHz), the length and time scales are extremely short.[1] Here this problem is exacerbated by both the 10 MHz order excitation frequency and the extremely high surface accelerations (see above). The micron and submicron order droplets are therefore ejected from the
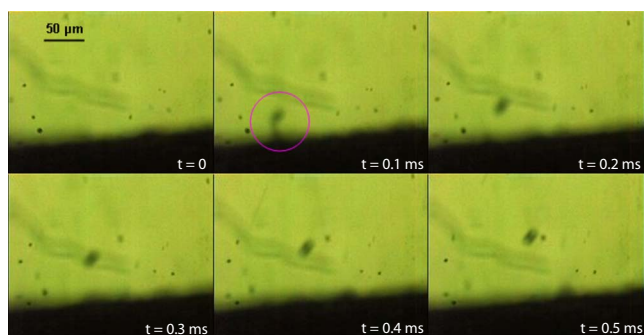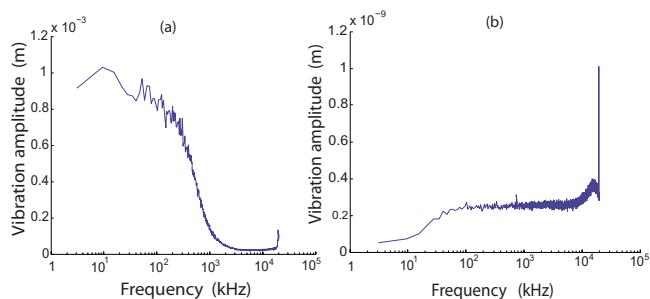

FIG. 3. (Color online) Drop deformation and atomization above a hydrophilic (bare lithium niobate) surface. The figure shows a sequence of images acquired at 10 000 frames/s and 5× magnification showing atomization of a drop which has spread into a thin film.

free drop surface at about 1 m/s, considerably higher than in other atomization processes; camera frame rates of 10 000 to 15 000 frames/s were barely sufficient to capture such events. Moreover, adequate illumination at these frame rates under magnification posed a challenge, not to mention the motion of the drop free surface out of the field of view during atomization. The images of the atomization events provided in this paper are therefore not of the quality that we would have desired but yet are of sufficient quality to allow us to propose qualitative and—to good approximation— *quantitative* models for the ejection and breakup mechanisms, employing scaling theory to guide the analysis.

We first consider the relevant length scales associated with the problem. The largest length scales are the characteristic dimension of the parent drop prior to spreading (that is, if spreading occurs), $R \sim 10^{-2}$–10^{-3} m, and the lateral dimension of the drop after it has spread into a thin film, $L \sim 10^{-3}$–10^{-4} m. The vertical length scale associated with the thickness of the fluid film is $H \sim 10^{-4}$–10^{-5} m. The length scales of both the ejected jet from the interfacial destabilization process and the ejected droplet during subsequent pinch-off corresponds to the capillary wavelength λ to be determined from the experiments and later corroborated with numerical simulation.

The relevant time scales are those associated with the excitation frequency $f = \omega/2\pi$ and the time required for capillary pinch-off. The former is specified by definition of the SAW device's IDT configuration, while the latter is the key question in this study. Unlike in previous work,[7,9,32,33] we do not assume *a priori* that these two time scales are of the same order. Instead, we chose to measure the frequency response of the capillary wave on the free surface of a water drop using a dc 40 MHz scanning laser Doppler vibrometer (MSA-400, Polytec GmBH, Waldbrünn, Germany), the results of which are shown in Fig. 4(a) in which the drop is being excited at 20 MHz. Though broadband excitation of capillary waves is obvious in the plot, there is no capillary wave at one-half the excitation frequency $f/2 \sim 10$ MHz nor even at the excitation frequency $f \sim 20$ MHz. Simply put, the capillary waves on the free surface of the drop do not undulate at these frequencies, and the presumption in prior work

would therefore appear to be in error if applied to our system. Instead, the majority of the capillary wave response is centered around 10 kHz, the peak in Fig. 4(a). This is comparable to the results of Eq. (3), suggesting that the surface waves are dominated by a balance between capillary and viscous stresses. This result is not especially surprising, since much of the SAW energy that is diffracted into the drop from the solid-fluid interface is dissipated through viscous stresses that manifest as acoustic streaming,[38] giving rise to bulk liquid recirculation within the drop.

Given the huge accelerations of the substrate as the SAW passes underneath the drop, the effects of fluid inertia might be expected to be significant. However, inertia is important only within a thin boundary layer adjacent to the substrate along which the SAW propagates. The thickness of the boundary layer typically scales as[39]

$$\delta \sim \left(\frac{\mu}{\rho \omega} \right)^{1/2}, \tag{5}$$

typically $0.1-1$ μm, more than one order of magnitude smaller than the characteristic drop/film thickness used in our study. The time scale associated with this inertial forcing due to the substrate acceleration is on the order of the excitation frequency f. In fact, if we allow the water film to evaporate until only a *very* thin layer is left behind, a second capillary wave resonance frequency appears at a frequency close to the excitation frequency, as shown in Fig. 4(b) (the sharp peak observed is significantly larger than signal noise, which is evident at lower frequencies); if the fluid film thins to a thickness commensurate with the boundary layer thickness δ, the response at this second resonance frequency will become dominant. In this case, it is possible to replace the relevant length scale R in the capillary-inertia frequency scaling in Eq. (4) with $H \sim \delta \sim 10^{-6}-10^{-7}$ m, such that $f_c \sim 1-10$ MHz $\sim f$, consistent with the resonant frequency peak in Fig. 4(b). Under these extraordinary conditions—SAW driven excitation of a fluid film with a thickness on the same order as the boundary layer in Eq. (5)—atomization occurs such that $f \sim f_c$ holds. Even in this situation, the modification to Kelvin's equation given in Eq. (2) is unwarranted. Kelvin's equation, Eq. (1), still holds as long as one appreciates that the capillary resonance frequency f_c used in Eq. (1) is that associated with capillary-inertia resonance in Eq. (4) instead of viscous-capillary resonance in Eq. (3).

This hypothesis is further verified by conducting the atomization experiments with glycerol (1 ml/ml, $\mu \sim 1.5$ kg/m s, $\rho \sim 1200$ kg/m³, $\gamma \sim 64$ mN/m) instead of water; the initial drop volume used is the same as that employed in our experiments with water. Due to the hydrophilicity of glycerol on the substrate, the glycerine spread into a thin film. Replacing the characteristic length scale with the film height $H \sim 10$ μm, the capillary-viscous resonant frequency given by Eq. (3) for the glycerine drop is approximately 1 kHz, whereas the capillary-inertia resonant frequency, as stipulated by Eq. (4), is on the order of 100 kHz. From Eq. (5), we estimate the boundary layer thickness δ to be approximately 10^{-5} m, which is typically on the same order as the film thickness. Following our assertion that the

Kelvin equation, i.e., Eq. (1), be employed by using a capillary resonant frequency f_c specified by the capillary-inertia resonant frequency, we predict an instability wavelength λ close to 10^{-5} m, which is roughly the same order as the $2-3$ μm droplet diameters observed experimentally. If the capillary-viscous resonant frequency were to be used instead, we would have obtained a prediction that is one order of magnitude larger than that observed.

In the case of finite-thickness thin films ($\delta \ll H \ll L$), which is the relevant case in our investigation, however, the flow is entirely viscous outside the boundary layer and occurs at a much slower time scale than that defined by the inverse of the excitation frequency.[38,40–42] This rules out the dominance of inertial forcing at the free surface and suggests that the appropriate capillary resonance frequency to use in Eq. (1) is the viscous-capillary resonance frequency in Eq. (3). The relevant time scale associated with jet formation and droplet pinch-off arising due to the destabilization of the capillary waves at the free surface of the parent drop is therefore the capillary-viscous pinch-off time scale defined by the inverse of the capillary-viscous resonance frequency in Eq. (3),[43,44] on the order $10^{-3}-10^{-4}$ s. We will employ this scaling subsequently in order to estimate the capillary wavelengths associated with jet formation and droplet pinch-off in our numerical simulations in Sec. III.

C. Destabilization mechanisms

We begin by considering the largest length scale associated with the problem, the drop dimension R, and the largest phenomena associated with this length scale that we were able to observe. At the tip of the deformed, conically shaped drop, a large crest is formed (see, for example, the last frame of Fig. 2). The length scale of this crest is, however, much larger than typical capillary wavelengths λ as it is associated with the entire fluid drop. Figure 5 shows the formation and subsequent elongation of the crest under high magnification and frame rates. Here, the SAW radiation is propagating from left to right in the image. We note that the angle at which the crest is inclined is close to the Rayleigh angle, 23° in our configuration, strongly suggesting that the crest is formed from acoustic streaming due to the SAW diffracted into the drop at this same angle, as illustrated by Figs. 5(a)–5(c). Subsequent images in Fig. 5 show that the wholesale undulation of the free surface leads to whipping of the elongated crest and its pinch-off to form a large droplet. On the rising half-cycle of the wave motion along the drop surface, the tip of the elongated crest is seen to be whipped backwards to the left [Figs. 5(d)–5(f)]. On the subsequent half-cycle in which the free surface is falling, the undulation of the free surface has traveled forward to the right, causing a subsequent thinning in the neck of the crest [Figs. 5(g)–5(i)] which finally pinches off to form a large drop [Figs. 5(j)–5(l)]. The time between Figs. 5(a) and 5(l) is approximately 1 ms, which provides further confirmation that the surface capillary waves are excited at 1 kHz order frequencies. Given the occurrence of these phenomena on the length scale of the drop R, it is not surprising that the ejected droplet is also large, on the order of 300 μm. Because of its
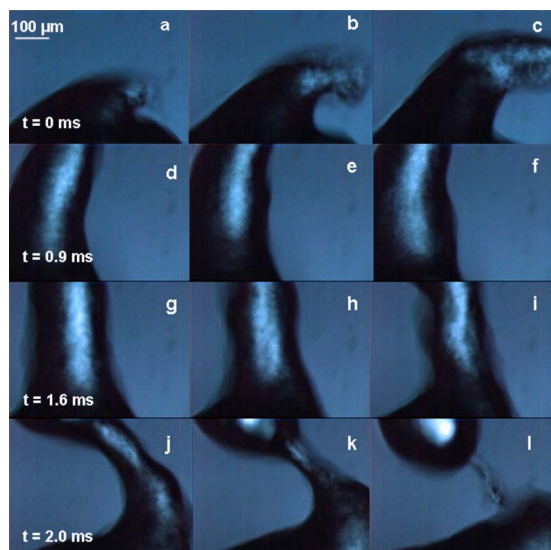
FIG. 5. (Color online) Sequence of images taken at 10 000 frames/s showing the formation of a crest at the tip of an elongated drop on a hydrophobic substrate (Fig. 2) due to SAW irradiation. The crest is whipped outwards and upwards on the rise half-cycle of a traveling capillary wave on the free surface. On the fall half-cycle, the forward propagation of this wave essentially leaves the tail of the elongated crest behind, thinning the thread and resulting in pinch-off to form a large 300 μm droplet. Due to its mass and low ejection velocity, this droplet falls back and recombines with the parent drop (not shown). The time between successive images in each row is 10^{-4} s; however, the first image in each row is taken at the times shown.
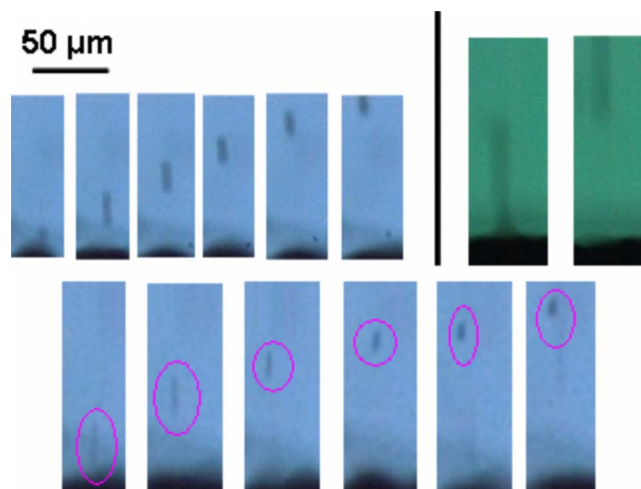

FIG. 6. (Color online) Three separate instances of jetting phenomena from the free surface of a thin film. The liquid thread that forms the axisymmetric jet arising due to the destabilization of a capillary wave on the free surface elongates and pinches-off near the base to form an ejected droplet. The velocity of the jet is roughly of the order 1 m/s but the droplet velocity, upon pinch-off, is much slower, approximately 0.1 m/s. The images were acquired at 10 000 frames/s and, hence, the time between successive images is 10^{-4} s for all cases.

size, the ejection speed is low and gravity is still significant, causing it to quickly redeposit back onto the parent drop and recombine. Such large droplet formation can occasionally be seen but is not a part of the drop atomization spectra due to the recombination.

A shorter length scale breakup phenomenon consists of the formation of axisymmetric jets and their subsequent pinch-off to form ejected droplets. As seen in Fig. 2—especially the frames at $t'=0$ ms and $t'=1$ ms in Fig. 2—the rapid and violent destabilization of the capillary waves at the free surface leads to the formation of liquid threads. As these threads elongate and thin, they eventually pinch off to form an ejected droplet as shown in frames $t'=2$ ms and $t'=3$ ms in Fig. 2, with a dimension that is of the same order as the jet diameter R, approximately 10 μm. Similar jetting phenomena are observed for capillary wave destabilization along the free surface of a fluid film, as shown in Fig. 6. Here, the jet diameter and, hence, the dimension of the ejected drop are slightly smaller, between 1 and 10 μm. The jet velocity U in both cases is initially large, on the order of 1 m/s, but much of its inertial energy is lost to viscous dissipation as the liquid thread drains and pinches off at its neck to form an ejected droplet, and by the time the droplet is ejected, its velocity is approximately 0.1 m/s. The pinch-off mechanism is akin to the classical Rayleigh–Plateau instability for the longwave axisymmetric breakup of a cylindrical liquid column.[45,46] Due to interfacial tension, the liquid column is unstable to axisymmetric perturbations with wavelengths several times larger than the radial dimension of the column.

A dominant balance between capillary and inertial

stresses then yields for the breakup length of the column (the length of the liquid column above which it becomes unstable)

$$L \sim \left(\frac{\rho U^2 R^3}{\gamma} \right)^{1/2} \sim 10^{-5} \; \mu\text{m}, \qquad (6)$$

consistent with the first two image frames in Fig. 6. In contrast, the time it takes for the liquid thread to drain and pinch off, typically 10^{-4} s, is in agreement with the viscous-capillary pinch-off time scale in Eq. (3), suggesting the dominance of viscous and capillary stresses over inertial stress in the film drainage process.[43,44] We also note that, unlike the pinch-off of threads into multiple satellite droplets in ink-jet printers (see, for example, Ref. 1), only one or, at most, two droplets form here. This is due to the much higher velocity of the jet here such that the pinch-off occurs close to the base of the thread soon after its formation.

The size of the ejected drops, on the same order as the radial dimension of the jet, depends on the wavelength of the disturbances induced along the free surface λ; these appear to be around $1-10$ μm in the experimental results. As discussed in Sec. I, a linear stability analysis is not possible, and so a theoretical prediction of the critical instability wavelengths can only be obtained from a full nonlinear analysis to be carried out in the next section. Even so, a simple scaling argument arising from a viscous-capillary force balance is provided here to predict the instability wavelength. We note that the capillary stress has to be adjusted to account for the dominance of the axial capillary stress $\gamma(\partial^2 H / \partial x^2)$ over the azimuthal capillary stress γ/H for a thin film of thickness H and, hence, the viscous-capillary force balance reads
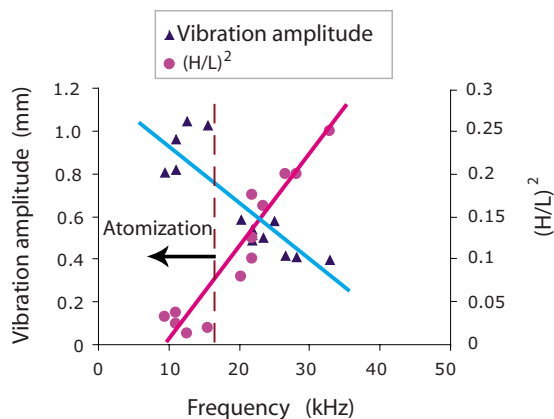
FIG. 7. (Color online) Variation in the amplitude of the capillary wave on the free surface of a liquid film with the frequency, which is a function of the film aspect ratio H/L. The onset of atomization occurs around 10 kHz.

$$\frac{\gamma H}{L^2} \sim \frac{\mu U}{H}, \tag{7}$$

where $U \sim \lambda f$ is the wave velocity. Rearranging then gives

$$\lambda \sim \frac{\gamma H^2}{\mu f L^2} \tag{8}$$

for the instability wavelength, which is roughly $1-10$ μm, in approximate agreement with the jet and droplet dimensions observed in the experiments.

Figure 7 shows the dependence of the peak capillary resonance frequency on the square of the film aspect ratio H/L. For a given instability wavelength, we note from Eq. (8) that $f \sim (H/L)^2$, consistent with the trends in Fig. 7. In the same figure, the peak amplitude of the capillary waves is plotted as a function of the frequency, obtained using measurements from the laser Doppler vibrometer. Initially, the vibration amplitude is about 400 μm at a peak capillary resonance frequency of around 30 kHz; though the capillary wave can be seen and measured, no atomization occurs. Over time, exposure to the SAW causes the film to thin and the peak capillary resonance frequency to decrease. The film aspect ratio drops, the peak capillary resonance frequency falls, and the vibration amplitude at this peak capillary resonance frequency increases until there is a sharp increase in vibration amplitude and drop in the aspect ratio at just over 15 kHz. This is associated with the onset of atomization, as predicted by Eq. (3), at around 10 kHz, lending further support to the assertion that the relevant frequency scale is the capillary resonance frequency instead of the applied frequency of the SAW device, as discussed in Sec. I. In fact, the droplet sizes are observed from the scaling theory above to depend predominantly on a balance between viscous and capillary stresses due to the rate limiting step imposed by the drainage and rupture of the liquid threads during the pinch-off process.

It should be noted that Fig. 7 does not suggest that the onset of atomization is frequency dependent. We postulate that the *instability wavelength* is dependent on the *viscous-capillary resonance frequency* (at least for finite-thickness drops and films), as stipulated by Eq. (8), which, in turn,

determines the size of the droplets ejected. The onset of atomization, or the *instability threshold*, on the other hand, depends crucially on a critical value of the *acoustic capillary number*, which we shall discuss further in the next section. Adequately large inertial stresses due to the acoustic forcing are required to overcome the stabilizing capillary stresses in order to sufficiently destabilize the interface such that atomization ensues. In the case of the experiments associated with Fig. 7, the input power was fixed throughout. As the film successively thins, the axial capillary stress decreases concomitantly (and hence the observed growth in the vibration amplitude for a given power input) until it is exceeded by the inertial stress whose value is fixed by the constant acoustic forcing, at which point, the interface can no longer be stabilized and atomization occurs. The results of Fig. 7, however, show that the peak capillary resonance frequency, which sets the instability wavelength, is dependent on the film thickness.

III. NUMERICAL SIMULATION

Though the experimental results together with scaling theory help identify, qualitatively, the mechanisms underlying the atomization process due to SAW irradiation, computational analysis of the fluid behavior would help present these mechanisms from another perspective, one where we have complete control over the conditions governing the destabilization process. We begin below by formulating the problem in the lubrication approximation for a thin film and follow through to numerically solve the nonlinear equation governing the spatiotemporal evolution of the film interfacial height driven by the SAW irradiation beneath, which, when sufficiently strong, overcomes the stabilizing capillary stresses and, hence, leads to the destabilization of the interface and subsequent atomization. We note that our simple lubrication model cannot capture the evolution of the interface right through to pinch-off and atomization due to the difficulty in resolving the increasingly singular spatial derivatives at the crests and troughs of the destabilized waves; nevertheless, the numerical simulation is able to predict important information regarding the destabilization process, for example, the critical acoustic capillary number and the capillary wavelength beyond which the film becomes unstable, which can then be employed for comparison with the experimental observations and against the postulated mechanisms and scaling arguments above.

A. Governing equations

As shown in Fig. 8, we consider a two-dimensional representation of a thin incompressible Newtonian liquid film in the shape of a slender drop with initial length L and height H in rectilinear coordinates $(x, 0, z)$, x being the axial coordinate and z the vertical coordinate. The density and viscosity of the liquid are denoted by ρ and μ, respectively. Given that $H \sim 10^{-4} - 10^{-5}$ m and $L \sim 10^{-3} - 10^{-4}$ m in our experiments, it is not unreasonable to assume that the film is sufficiently thin such that its aspect ratio can be described by a small parameter $\epsilon \equiv H/L \ll 1$. The film is bounded from below by a
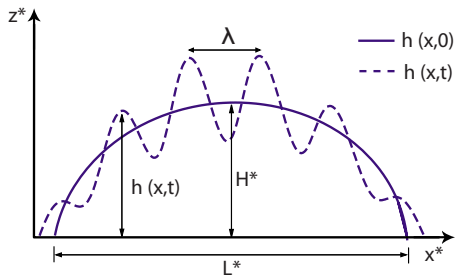
FIG. 8. (Color online) Schematic representation of the destabilization of an initial slender sessile drop with height H and length L. The initial drop profile is given by the solid line whereas the destabilized drop is given by the dashed line. The spatiotemporal film height distribution is given by $h(x,t)$, whereas the wavelength of the capillary waves is λ.

horizontal, infinitely long, rigid solid substrate at $z=0$ but is allowed to evolve freely at the air-liquid interface at $z=h$, where $h(x,t)$ is the thickness of the film.

The hydrodynamics of the incompressible liquid film is then governed by the equations of conservation of mass and momentum

$$\frac{\partial u}{\partial x} + \frac{\partial v}{\partial z} = 0, \tag{9}$$

$$\rho\left(\frac{\partial u}{\partial t} + u\frac{\partial u}{\partial x} + v\frac{\partial u}{\partial z}\right) = -\frac{\partial p}{\partial x} + \mu\left(\frac{\partial^2 u}{\partial x^2} + \frac{\partial^2 u}{\partial z^2}\right), \tag{10}$$

and

$$\rho\left(\frac{\partial v}{\partial t} + u\frac{\partial v}{\partial x} + v\frac{\partial v}{\partial z}\right) = -\frac{\partial p}{\partial z} + \mu\left(\frac{\partial^2 v}{\partial x^2} + \frac{\partial^2 v}{\partial z^2}\right), \tag{11}$$

where u and v are the axial and vertical velocities, t the time, and p the pressure in the film. The following no-slip boundary condition applies to the substrate $z=0$:

$$u = v = 0. \tag{12}$$

These are complemented by the interfacial boundary conditions governing the continuity of tangential stresses and the jump in the normal stresses across the interface at $z=h$,

$$\frac{\partial u}{\partial z} + \frac{\partial v}{\partial x} = 0 \tag{13}$$

and

$$p = \gamma\kappa + p_A, \tag{14}$$

where

$$\kappa = -\frac{\partial^2 h}{\partial x^2} \tag{15}$$

is twice the mean curvature of the slender drop interface and p_A is the acoustic pressure, which we will define below. We neglect any disjoining pressure effects as we are not concerned with the spreading of the drop but rather the deformations along its interface arising due to the acoustic forcing. Closure to the above set of equations is provided by the kinematic boundary condition applied to the interface at $z=h$,

$$\frac{\partial h}{\partial t} + \frac{\partial(h\bar{u})}{\partial x} = v, \tag{16}$$

where

$$\bar{u} = \frac{1}{h}\int_0^h u\, dy \tag{17}$$

is the cross-sectional average velocity across the height of the film.

As an approximation in this simplified theory, we will model the acoustic pressure forcing as a traveling wave along the interface that is excited by the SAW vibration on the substrate,[47]

$$p_A = \rho u_s^2, \tag{18}$$

where u_s is the velocity of a particle element on the substrate as the SAW propagates across it. Since the displacement of this particle element can be written as $A\cos\theta_R e^{jkx}e^{j\omega t}$, where A is the vibration amplitude of the SAW, θ_R the Rayleigh angle, k the wave number, and ω the angular frequency, it then follows from above that

$$p_A = -\rho\omega^2 A^2 \cos^2\theta_R e^{2jkx}e^{2j\omega t}. \tag{19}$$

We note that Eqs. (18) and (19) should contain a multiplier that allows for the decay of the SAW radiation into the fluid. Nevertheless, we will neglect this multiplier since it is a unit order coefficient for the case of a thin film.

B. Scaling and dimensionless equations

We adopt the following set of scalings to render the governing equations dimensionless:

$$x^* \equiv \frac{x}{L}, \quad (z^*,h^*) \equiv \frac{(z,h)}{H}, \quad u^* \equiv \frac{u}{U},$$

$$v^* \equiv \frac{v}{\epsilon U}, \quad t^* \equiv \frac{t}{L/U}, \quad p^* \equiv \frac{p}{\epsilon\gamma/L}, \tag{20}$$

where $U \equiv \epsilon^3\gamma/\mu$ is the characteristic velocity scale obtained from a balance between capillary and viscous stresses, consistent with our assertion in Sec. II B that these stresses dominate over inertial stresses in the bulk region away from the boundary layer. We also choose this particular scaling to demote the pressure to the same order as the capillary stress such that the relative contributions of the acoustic and capillary stresses can be described[48] by a single dimensionless parameter—the *acoustic capillary number*—which will be defined subsequently. In the above, the asterisks denote dimensionless quantities.

Substituting the set of scalings above into the governing equations in Sec. III A and dropping the asterisk decorations henceforth then leads to the following set of equations to leading order as $\epsilon \to 0$:

$$\frac{\partial u}{\partial x} + \frac{\partial v}{\partial z} = 0, \tag{21}$$

$$\frac{\partial p}{\partial x} = \frac{\partial^2 u}{\partial z^2}, \tag{22}$$

and

$$\frac{\partial p}{\partial z} = 0, \tag{23}$$

with the following boundary conditions:

$$u = 0 \quad \text{and} \quad v = 0 \quad \text{at } z = 0, \tag{24}$$

$$\frac{\partial u}{\partial z} = 0 \quad \text{at } z = h, \tag{25}$$

$$p = -\frac{\partial^2 h}{\partial x^2} - C e^{2j\tilde{k}x} e^{2j\tilde{\omega}t} \quad \text{at } z = h, \tag{26}$$

and

$$\frac{\partial h}{\partial t} + \frac{\partial (h\bar{u})}{\partial x} = 0 \quad \text{at } z = h. \tag{27}$$

In the above,

$$C \equiv \frac{\rho \omega^2 A^2 \cos^2 \theta_R L}{\epsilon \gamma} \tag{28}$$

represents an acoustic capillary number that quantifies the relative magnitudes between the applied acoustic stress and the capillary stress, while $\tilde{k} \equiv kL$ and $\tilde{\omega} \equiv \omega L/U = \mu \omega L/\epsilon^3 \gamma$ are the dimensionless wave numbers and frequencies, respectively.

Integrating Eq. (22) with the boundary conditions given by Eqs. (24) and (25) then gives the following parabolic velocity profile in the film:

$$u = \left(\frac{z^2}{2} - hz\right)\frac{\partial p}{\partial x}. \tag{29}$$

Cross-sectional averaging of Eq. (29) and substitution into the kinematic boundary condition given by Eq. (27) gives the following evolution equation for film thickness:

$$\frac{\partial h}{\partial t} = \frac{1}{3}\frac{\partial}{\partial x}\left(h^3 \frac{\partial p}{\partial x}\right), \tag{30}$$

with the pressure specified by Eq. (26).

C. Initial and boundary conditions

Initially, the profile of the undeformed drop prior to the application of the acoustic forcing can be approximated by the following initial condition:

$$h(x,0) = e^{-x^2/0.05}. \tag{31}$$

This arbitrarily imposed drop initial profile is not important since we leave the contact line unpinned so that the drop is allowed to spread to an equilibrium profile governed by the curvature within a short initial transient once the simulation commences.[49]

The following boundary conditions are also imposed:

$$\left.\frac{\partial h(x,t)}{\partial x}\right|_{x\to-\infty, x\to\infty} = \left.\frac{\partial h(x,0)}{\partial x}\right|_{x\to-\infty, x\to\infty} \tag{32}$$

and

$$\left.\frac{\partial^3 h(x,t)}{\partial x^3}\right|_{x\to-\infty, x\to\infty} = \left.\frac{\partial^3 h(x,0)}{\partial x^3}\right|_{x\to-\infty, x\to\infty}. \tag{33}$$

D. Numerical method

We numerically solve the fourth-order nonlinear parabolic partial differential equation governing the spatiotemporal evolution of the drop height given by Eq. (30) together with the acoustic forcing pressure in Eq. (26), subject to the initial and boundary conditions stipulated by Eqs. (31)–(33) using MATHEMATICA (Wolfram Research, Champaign, IL), which employs an adaptive method of lines[50] to facilitate solution via transformation of the nonlinear partial differential equations into a system of ordinary differential equations; fourth-order centered differences were utilized to discretize the spatial coordinates. Fortunately the initial conditions permit expression of the problem as a Cauchy system; we chose a spatial mesh density of 300 points laid out in an adaptive grid across three dimensionless units from −1.5 to 1.5 based on an *a priori* spatial error estimate determined via Richardson extrapolation using the initial conditions.[51] The locations of the spatial discretization points are subsequently fixed during the progression of the analysis because changing them necessitates a complete and impractical restart of the ordinary differential equation system solution process. The time stepping is determined by an *a priori* error estimate based on a Richardson extrapolation of the initial condition. Given both the inherent stiffness of the nonlinear equations of motion and their extreme sensitivity to the proposed initial conditions, we choose a relatively advanced implicit Euler method, the Radau IIA implicit Runge–Kutta method,[52] for the solution of the temporal evolution of the ordinary differential equation system. After solving these equations, an *a posteriori* spatial error estimate is made on the solution found at the final time step to ensure that the adaptive spatial discretization has remained appropriate throughout the course of the temporal solution process.

Since the pressure wave induced by the SAW at the solid-fluid interface has a constant frequency (20 MHz) and nearly constant wavelength (200 μm; the fluid-loaded and air-loaded wavelengths differ by about 5%), it then follows that the dimensionless wave number and frequency are fixed, i.e., $\tilde{k} \equiv kL = 2\pi L/\lambda = 10\pi$ and $\tilde{\omega} = \mu \omega L/\epsilon^3 \gamma \sim 10^7$. The only remaining parameter is the acoustic capillary number C defined by Eq. (28), which we shall vary between 10^{-3} and 10^{-1} in our numerical simulations.

As is commonly carried out in lubrication models,[53] the computations are halted when the capillary wave deformations grow to an amplitude similar to the drop height due to the increasingly singular spatial derivatives at the crests and troughs of the destabilized waves. Since the deformations at this point are larger than that observed experimentally, it is not unreasonable to assume that, beyond this point, the interface is sufficiently destabilized such that jet formation and
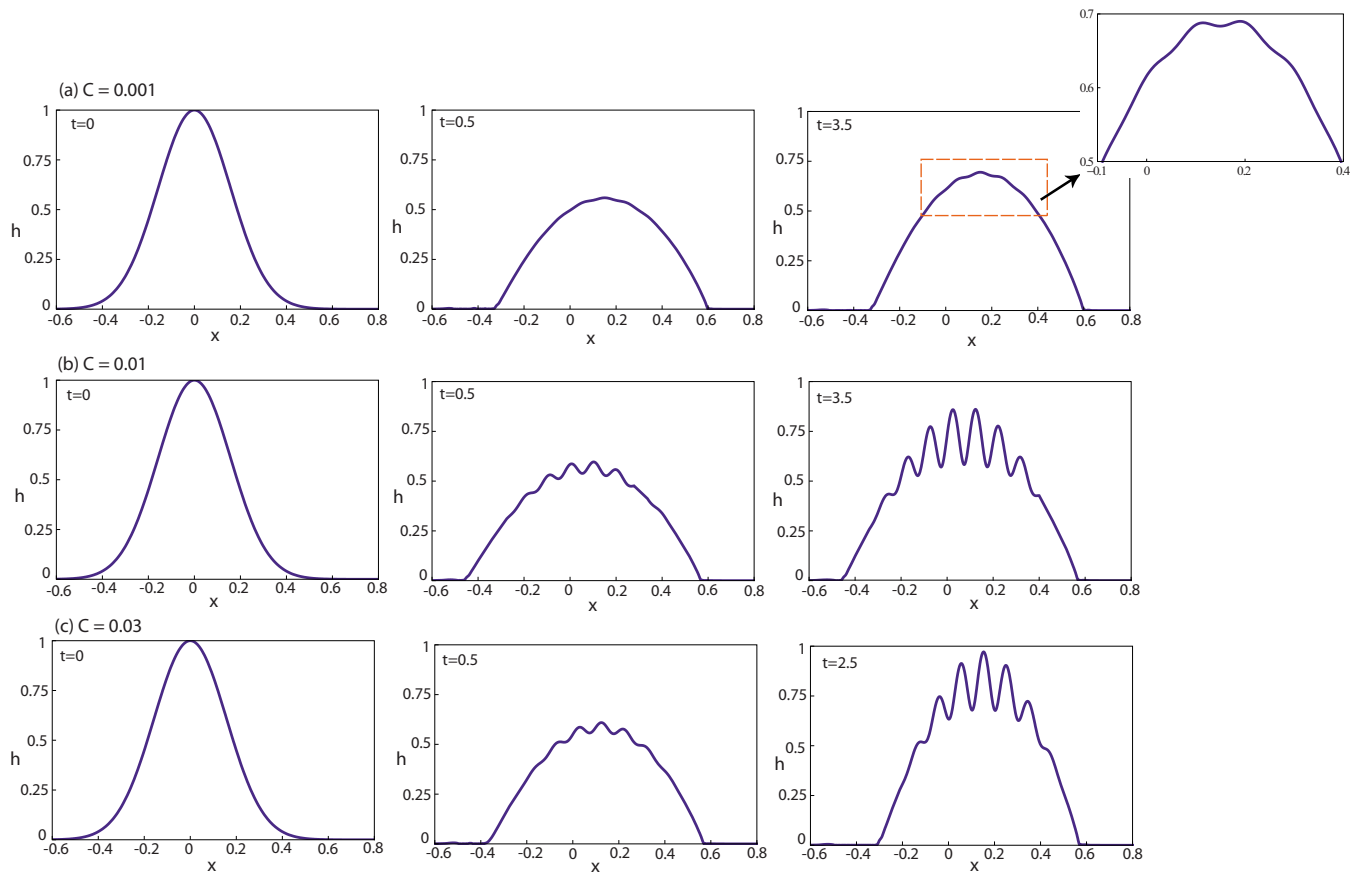
FIG. 9. (Color online) Drop interfacial profiles at various dimensionless times for (a) $C=0.001$, (b) $C=0.01$, and $C=0.03$. The dimensionless wave number $\tilde{k}$ and frequency $\tilde{\omega}$ are held at 10π and 10^7, respectively. The initial drop profile (first frame) relaxes to its equilibrium position and translates a short distance to the right in the direction of propagation of the imposed traveling acoustic pressure wave (second frame). During this initial transient, interfacial waves are observed to appear, induced by the pressure wave. In the final frame, these interfacial undulations remain stable due to insufficient acoustic forcing to overcome the stabilizing capillary forces, as shown in the inset for small C values in case (a), or are rapidly destabilized for C values beyond a critical threshold leading towards atomization in cases (b) and (c). The critical threshold for interfacial destabilization therefore lies somewhere around $C=0.01$.

pinch-off proceed, leading to atomization. Though we are unable to directly model the latter phenomena with the simple lubrication model, it is possible to estimate a critical acoustic capillary number that describes the transition from simple capillary wave generation to atomization. Moreover, the numerically predicted destabilization wavelengths provide another rough indication of the dimensions of the atomized droplets that can be compared to the experimentally measured droplet dimensions as well as those predicted from our scaling theory above. For these purposes, the simple model is sufficient as a first approximation for corroborating the hypotheses postulated in Sec. II.

E. Results and discussion

Figure 9 illustrates the spatiotemporal evolution of the drop profile for three values of the acoustic capillary number, i.e., $C=0.001$, $C=0.01$, and $C=0.03$, respectively. It can be seen that the initial drop interfacial profile in the first frame quickly relaxes to its equilibrium shape and translates a small distance in the direction in which the imposed interfacial traveling pressure wave propagates (second frame), all within an initial transient $t<0.1$. We note that the translation is not an artifact of the numerical solution; we have demonstrated rapid translation of sessile drops sitting atop sub-

strates along the direction of propagating SAWs.[15] For small acoustic capillary numbers ($C \lesssim 0.001$) wherein the capillary stress is dominant over the acoustic forcing, the interfacial deformation is small and stable, as observed in the second and final frames (see also the inset) in Fig. 9(a). Above a critical acoustic capillary number ($C \sim 0.01$), the pressure wave induces an apparent capillary wave at the interface (second frame), which then rapidly grows in amplitude. In this case, the large acoustic irradiation is acting as a destabilizing effect on the free surface beyond the stabilizing and restoring effect of the capillary force, causing the interfacial wave to grow unabated (final frame), as shown in Figs. 9(b) and 9(c). As the value of C is increased, the time required to destabilize the interface becomes shorter.

The critical acoustic capillary number beyond which the interface is destabilized is more easily seen when plotting the energy of the wave,[54,55]

$$E(t) = \int_{-\infty}^{\infty} h^2(x,t)dx - \int_{-\infty}^{\infty} h^2(x,0.5)dx, \quad (34)$$

the second term at $t=0.5$ representing the energy of the interface after the drop has initially spread to its equilibrium position. The energies corresponding to the drop profiles for
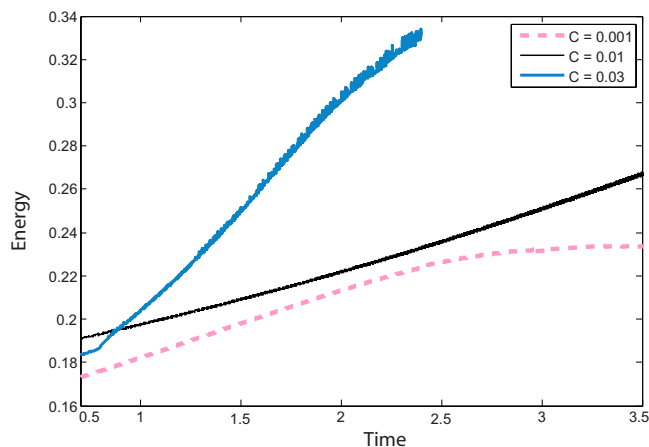
FIG. 10. (Color online) Drop interfacial energy E defined by Eq. (34) as a function of time for various acoustic capillary numbers C. The other parameters are $\tilde{k}=10\pi$ and $\tilde{\omega}=10^7$.

the different cases in Fig. 9 are then plotted in Fig. 10. For small values of C below 0.01, the energy is initially observed to grow in response to the acoustic irradiation from the SAW. However, since this is insufficient to overcome the restoring capillary force, the energy reaches a plateau, suggesting that the disturbance is stabilized as observed by the small undulations in the inset of the third frame in Fig. 9(a). However, as C is increased to 0.01, this plateau disappears quite suddenly and the energy is seen to increase monotonically; as the acoustic irradiation is increased beyond a critical value, approximately $C \sim 0.01$, such that the stabilizing action of the capillary stresses is overcome, the capillary wave disturbance grows without bound. As C is further increased, we observe the energy held in the capillary wave motion to increase exponentially, at least qualitatively, at a given time and to grow in amplitude with respect to time at a far faster rate, illustrating the rapid and explosive growth of the interfacial disturbance beyond a critical value of the excitation energy provided by the SAW irradiation. Here, we propose that the critical acoustic capillary number can be estimated at the onset of inflection in the growth energy curves.

In this case, the critical acoustic capillary number is approximately 0.01. This is the correct order of magnitude if we compare it to the critical acoustic capillary number calculated from Eq. (28) with the use of experimental values which lead to the onset of atomization. An approximation for the dimension of the atomized droplet can also be estimated from the observed instability wavelength λ. From Figs. 9(b) and 9(c), we observe λ to be approximately a tenth of the drop dimension. Since $L \sim 10^{-3}-10^{-4}$ m, it then follows that $\lambda \sim 10~\mu$m, on the same order as both the value predicted by the dominant viscous-capillary balance in Eq. (8) and that observed in the experimental observations, as reported in Sec. II. The close agreement between the predictions afforded by our simple model and the experimental results for both the critical acoustic capillary number and the droplet dimension therefore lends confidence to our hypotheses in Sec. II, especially our claim that the capillary wave on the drop surface and its subsequent destabilization to form atom-

ized droplets are governed by viscous-capillary dominated interfacial effects under acoustic forcing, not a subharmonic half-excitation frequency relationship.

IV. CONCLUSIONS

The atomization process driven by SAWs is exceptionally complex, occurring over multiple length and time scales, many of which are difficult to observe in the laboratory. As such, little of the underlying mechanisms responsible for the destabilization of the interface leading towards breakup and ejection of the atomized droplets is truly understood. In this paper, we have attempted to elucidate the mechanisms underlying the atomization phenomenon obtained via 10 MHz order acoustic excitation through a combination of experiments, scaling analysis, and simple numerical modeling. This arrangement has exposed problems in the current interpretation of the atomization phenomenon that has been developed over the years, and we conclude that revisiting the problem with a proper appreciation of the various length and time scales inherent to the physics of the system is crucial to understanding why the currently accepted theory is giving such remarkable errors and in helping to cast a new view of the phenomenon.

A longstanding misconception that has led to erroneous predictions of droplet sizes is the modification of the Kelvin equation by replacing the frequency of the capillary wave f_c with one-half of the excitation frequency f, with the presumption that the capillary waves are subharmonic Faraday waves. This modified equation has often been used to estimate the wavelength of the capillary waves, and we show through experimental measurements of the capillary wave frequency via scanning laser Doppler vibrometry that this is incorrect; instead, the capillary waves at the drop free surface vibrate at frequencies on the same order as the capillary-viscous resonant frequency $f_c \sim \gamma/\mu R$. For modest ultrasonic excitation ($\sim 10-100$ kHz), where $f \sim f_c$, this may not lead to significantly erroneous predictions, but when the excitation occurs at high frequencies, i.e., $f \gg f_c$, it then becomes obvious that the deviation becomes increasingly large.

Furthermore, we also consider very thin fluid films where inertial effects are indeed relevant and find in this remarkably rare arrangement that both the excitation and capillary wave frequencies are on the same order, rendering the modification to Kelvin's equation redundant. Nevertheless, the capillary wave vibration, in this case, is due to capillary-inertia resonance, i.e., $f_c \sim (\gamma/\rho H^3)^{1/2} \sim f$. In any case, we argue that it is the capillary wave frequency f_c that is the relevant frequency scale and, hence, the modification to the Kelvin equation to replace f_c with the excitation frequency f is fundamentally unnecessary. Instead, it is simply a matter of evaluating f_c either from the capillary-viscous frequency in the case $f \gg f_c$ or from the capillary-inertia frequency in the case $f \sim f_c$ to determine the droplet diameter and destabilization behavior.

We also relate the variety of observed droplet ejection phenomena to specific length-scale-dependent interfacial destabilization mechanisms. At the largest length scale, on the order of the dimension of the parent drop, large droplets are

whipped off the crest of the elongated drop at time scales corresponding to the viscous-capillary pinch-off time. At shorter length scales, the destabilization of the interfacial capillary waves leads to the formation of axisymmetric jets that elongate and subsequently pinch-off to form droplets. The pinch-off process occurs in a similar manner to the classical Rayleigh–Plateau instability for longwave axisymmetric breakup of cylindrical liquid columns; balancing capillary and inertial stresses within the jet results in a breakup length consistent with the experimental observations. Despite the role of the inertia of the jet, however, the pinch-off dynamics is governed by the time taken for film drainage, which is dominated by viscous drag. The dimensions of these ejected droplets, typically 10 μm, correspond to the jet diameter, which, in turn, coincides with the instability wavelength, consistently predicted by both the scaling argument developed from a dominant force balance between the viscous and capillary stresses and the numerical simulation of the spatiotemporal evolution equation governing the interfacial profile of a sessile drop along which a traveling acoustic pressure wave is excited. Finally, the numerical solutions predict a critical acoustic capillary number at the onset of interfacial destabilization that matches our experimental conditions.

Taken together, the multiple approaches to this difficult problem expose both the mechanisms underlying the fascinating phenomena of high-frequency acoustic atomization and ways in which they may be examined in the future, with a fortunately consistent explanation across experimentation, analysis, and numerics.

[1] O. A. Basaran, "Small-scale free surface flows with breakup: Drop formation and emerging applications," AIChE J. **48**, 1842 (2002).

[2] J. Friend, L. Yeo, D. Arifin, and A. Mechler, "Evaporative self-assembly assisted synthesis of polymeric nanoparticles by surface acoustic wave atomization," Nanotechnology **19**, 145301 (2008).

[3] L. Y. Yeo, Z. Gagnon, and H.-C. Chang, "AC electrospray biomaterials synthesis," Biomaterials **26**, 6122 (2005).

[4] A. M. Gañán-Calvo, "Generation of steady liquid microthreads and micron-sized monodispersed sprays in gas streams," Phys. Rev. Lett. **80**, 285 (1998).

[5] J. M. Grace and J. C. M. Marijnissen, "A review of liquid atomization by electrical means," J. Aerosol Sci. **25**, 1005 (1994).

[6] L. Y. Yeo, D. Lastochkin, S.-C. Wang, and H.-C. Chang, "A new AC electrospray mechanism by Maxwell–Wagner polarization and capillary resonance," Phys. Rev. Lett. **92**, 133902 (2004).

[7] R. J. Lang, "Ultrasonic atomization of liquids," J. Acoust. Soc. Am. **34**, 6 (1962).

[8] S. Ueha, N. Maehara, and E. Mori, "Mechanism of ultrasonic atomization using a multi-pinhole plate," J. Acoust. Soc. Jpn. **6**, 21 (1985).

[9] G. Forde, J. Friend, and T. Williamson, "Straightforward biodegradable nanoparticle generation through megahertz-order ultrasonic atomization," Appl. Phys. Lett. **89**, 064105 (2006).

[10] A. J. Yule and Y. Al-Suleimani, "On droplet formation from capillary waves from a vibrating surface," Proc. R. Soc. London, Ser. A **456**, 1069 (2000).

[11] A. J. James, B. Vukasinovic, M. K. Smith, and A. Glezer, "Vibration-induced drop atomization and bursting," J. Fluid Mech. **476**, 1 (2003).

[12] M. Kurosawa, T. Watanabe, A. Futami, and T. Higuchi, "Surface acoustic wave atomizer," Sens. Actuators, A **50**, 69 (1995).

[13] R. M. White and F. W. Volmer, "Direct piezoelectric coupling to surface elastic waves," Appl. Phys. Lett. **7**, 314 (1965).

[14] K. Y. Hashimoto, *Surface Acoustic Wave Devices in Telecommunications: Modelling and Simulation* (Springer, Berlin, 2000).

[15] M. K. Tan, J. R. Friend, and L. Y. Yeo, "Microparticle collection and concentration via a miniature surface acoustic wave device," Lab Chip **7**, 618 (2007).

[16] M. K. Tan, J. R. Friend, and L. Y. Yeo, *Proceedings of the 16th Australasian Fluid Mechanics Conference*, Gold Coast, Queensland, Australia, 3–7 December 2007, edited by P. Jacobs, P. McIntyre, M. Cleary, D. Buttsworth, D. Mee, R. Clements, R. Morgan, and C. Lemckert (University of Queensland, Brisbane, 2007), pp. 790–793.

[17] A. Wixforth, C. Strobl, Ch. Gauer, A. Toegl, J. Scriba, and Z. v. Guttenberg, "Acoustic manipulation of small droplets," Anal. Bioanal. Chem. **379**, 982 (2004).

[18] K. Sritharan, C. J. Strobl, M. F. Schneider, and A. Wixforth, "Acoustic mixing at low Reynold's numbers," Appl. Phys. Lett. **88**, 054102 (2006).

[19] R. Shilton, M. K. Tan, L. Y. Yeo, and J. R. Friend, "Particle concentration and mixing in microdrops driven by focused surface acoustic waves," J. Appl. Phys. **104**, 014910 (2008).

[20] M. K. Tan, J. Friend, and L. Yeo, "Direct visualization of surface acoustic waves along substrates using smoke particles," Appl. Phys. Lett. **91**, 224101 (2007).

[21] H. Li, J. R. Friend, and L. Y. Yeo, "Surface acoustic wave concentration of particle and bioparticle suspensions," Biomed. Microdevices **9**, 647 (2007).

[22] A. Wixforth, "Acoustically driven planar microfluidics," Superlattices Microstruct. **33**, 389 (2003).

[23] H. Li, J. R. Friend, and L. Y. Yeo, "A scaffold cell seeding method driven by surface acoustic waves," Biomaterials **28**, 4098 (2007).

[24] Lord Rayleigh, "On waves propagated along the plane surface of an elastic solid," Proc. London Math. Soc. **s1–s17**, 4 (1885).

[25] B. Vukasinovic, M. K. Smith, and A. Glezer, "Mechanisms of free-surface breakup in vibration-induced liquid atomization," Phys. Fluids **19**, 012104 (2007).

[26] W. T. Kelvin, "Hydrokinetic solutions and observations," Philos. Mag. **42**, 362 (1871).

[27] G. Taylor, "The instability of liquid surfaces when accelerated in a direction perpendicular to their planes. I," Proc. R. Soc. London, Ser. A **201**, 192 (1950).

[28] M. Faraday, "On a peculiar class of acoustical figures and on certain forms assumed by groups of particles upon vibrating elastic surfaces," Philos. Trans. R. Soc. London **121**, 299 (1831).

[29] P. Chen and J. Viñals, "Pattern selection in Faraday waves," Phys. Rev. Lett. **79**, 2670 (1997).

[30] J. Miles and D. Henderson, "Parametrically forced surface waves," Annu. Rev. Fluid Mech. **22**, 143 (1990).

[31] W. Eisenmenger, "Dynamic properties of the surface tension of water and aqueous solutions of surface active agents with standing capillary waves in the frequency range from 10 kc/s to 1.5 Mc/s," Acustica **9**, 327 (1959).

[32] M. Kurosawa, A. Futami, and T. Higuchi, *Transducers '97*, Proceedings of the 1997 International Conference on Solid-State Sensors and Actuators, Chicago, IL, 16–19 June 1997 (IEEE, Piscataway, NJ, 1997), Vol. 2, pp. 801–804.

[33] F. Barreras, H. Amaveda, and A. Lozano, "Transient high-frequency ultrasonic water atomization," Exp. Fluids **33**, 405 (2002).

[34] Y.-J. Chen and P. H. Steen, "Dynamics of inviscid capillary breakup: collapse and pinchoff of a film bridge," J. Fluid Mech. **341**, 245 (1997).

[35] T. B. Benjamin and F. Ursell, "The stability of the plane free surface of a liquid in vertical periodic motion," Proc. R. Soc. London, Ser. A **225**, 505 (1954).

[36] J. W. Miles, "Nonlinear Faraday resonance," J. Fluid Mech. **146**, 285 (1984).

[37] V. I. Sorokin, "The effect of fountain formation at the surface of a vertically oscillating liquid," Sov. Phys. Acoust. **3**, 281 (1957).

[38] W. L. Nyborg, *Acoustic Streaming* (Academic, New York, 1965).

[39] P. M. Morse and K. U. Ingard, *Theoretical Acoustics* (McGraw-Hill, New York, 1968).

[40] W. L. Nyborg, "Acoustic streaming due to attenuated plane waves," J. Acoust. Soc. Am. **25**, 68 (1953).

[41] M. Schindler, P. Talkner, and P. Hanggi, "Computing stationary free-surface shapes in microfluidics," Phys. Fluids **18**, 103303 (2006).

[42]M. Schindler, "Free-surface microflows and particle transport," Ph.D. thesis, University of Augsburg, 2006.

[43]J. Eggers, "Universal pinching of 3D axisymmetric free-surface flow," Phys. Rev. Lett. **71**, 3458 (1993).

[44]D. T. Papageorgiou, "On the breakup of viscous liquid threads," Phys. Fluids **7**, 1529 (1995).

[45]J. Plateau, "Statique expérimentale et théorique des liquides soumis aux seules forces moléculaires," Acad. Sci. Bruxelles Mem. **23**, 5 (1849).

[46]Lord Rayleigh, "On the capillary phenomena of jets," Proc. R. Soc. London **29**, 71 (1879).

[47]K. D. Frampton, S. E. Martin, and K. Minor, "The scaling of acoustic streaming for application in micro-fluidic devices," Appl. Acoust. **64**, 681 (2003).

[48]L. Y. Yeo and H. C. Chang, "Electrowetting films on parallel line electrodes," Phys. Rev. E **73**, 011605 (2006).

[49]L. Y. Yeo, O. K. Matar, and R. V. Craster, "Drop manipulation and surgery using electric fields," J. Colloid Interface Sci. **306**, 368 (2007).

[50]W. E. Schiesser, *The Numerical Method of Lines* (Academic, San Diego, 1991).

[51]B. Fornberg, *A Practical Guide to Pseudospectral Methods* (Cambridge University, Cambridge, 1996).

[52]N. Guglielmi and E. Hairer, "Implementing Radau IIA methods for stiff delay differential equations," Computing **67**, 1 (2001).

[53]L. Y. Yeo, O. K. Matar, E. S. Perez de Ortiz, and G. F. Hewitt, "The dynamics of Marangoni-driven local film drainage between two drops," J. Colloid Interface Sci. **241**, 233 (2001).

[54]O. K. Matar and S. M. Troian, "The development of transient fingering patterns during the spreading of surfactant coated films," Phys. Fluids **11**, 3232 (1999).

[55]L. Y. Yeo, R. V. Craster, and O. K. Matar, "Marangoni instability of a thin liquid film resting on a locally heated horizontal wall," Phys. Rev. E **67**, 056315 (2003).